Structural and Electrical Properties of 0.6 $Pb(Mg_{1/3}Nb_{2/3})O_3$–0.4 $PbTiO_3$ Ceramics

J.K. Mishra[a], K. Agrawal[b], S.K. Mohanty[c] and B. Behera[a,*]

[a] *School of Physics, Sambalpur University, Jyoti Vihar, Burla-768019, Odisha, India*
[b] *Department of Physics, Veer Surendra Sai University of Technology, Burla-768018, Sambalpur, Odisha, India*
[c] *Department of Physics, Kendrapara Autonomous College, Kendrapara-754 211, Odisha, India*

Received: 13.08.2021 & Accepted: 08.11.2021

Doi: 10.12693/APhysPolA.140.415 *e-mail: banarjibehera@gmail.com

$0.6Pb(Mg_{1/3}Nb_{2/3})O_3$–$0.4PbTiO_3$ ceramics are prepared by a mixed-oxide method and detail analysis of structural and electrical properties is carried out. The Rietveld refinement of X-ray diffraction data suggests that the compound has both a tetragonal and a cubic phase. From the complex impedance plots, the major effects of impedance are found, i.e., grain, grain boundary resistance and the presence of non-Debye type of relaxation. From the conductivity study, the ac conductivity is found to rise with temperature and the activation energy is found to be 0.71 eV.

topics: Rietveld, XRD, complex impedance, conductivity

1. Introduction

The ferroelectric $Pb(Mg_{1/3}Nb_{2/3})O_3$–$PbTiO_3$ (PMN–PT) combines the properties of relaxor ferroelectric (RFE) of $Pb(Mg_{1/3}Nb_{2/3})O_3$ and ferroelectric (FE) $PbTiO_3$ [1]. This single crystal near the morphotropic phase boundary (MPB) exhibits ultra high piezoelectric (PE) constant ($d_{33} \approx 2500$ pC/N and large electromechanical coupling coefficient (k_{33}) of about 0.9. Also, PMN–PT has large dielectric constant $\varepsilon_r \approx 3100$ and very less dielectric loss factor $\tan(\delta) \approx 0.014$ [2, 3]. Owing to these interesting properties of PMN–PT, perovskite single crystals have been widely used in the piezoelectric (PE) devices such as medical ultrasonic transducers and underwater acoustic transducer. Wang et al. [4] revealed that PMN–PT can be used for cost effective manufacturing; high-frequency ultrasonic devices can replace high-cost PE single crystals. Also, Tian et al. [5] reported the application of PMN–PT in an acoustic transducer. Zhou et al. [6] have synthesised a PMN–PT single crystal for ultrasonic transducer in biomedical application.

Recently, PE devices based on PMN–PT single crystals have attracted larger interest and made an outbreak in the field of electromechanical transducer. However, the applications associated with their excellent FE and pyroelectric properties of these multifunctional materials are highly desirable. PMN–PT is an ABO_3 pervoskite where A-site is occupied by Pb^{2+} ion with large radius while B-site is occupied by Mg^{2+}, Nb^{2+} and Ti^{4+} ion with a smaller radius. Thus, a complex PMN–PT solid system shows different properties, when the composition of PMN and PT is changed. When the PT concentration is increased in PMN–PT system, a phase transition from rhombohedral (R) to tetragonal (T) phase occurs. In certain composition, the regions of both R and T phase coexist. Also, the increase in concentration of PT leads to reduction in the relaxor effect of PMN and tends to vanish. It is believed that MPB of $(1-x)$PMN-xPT system at room temperature (RT) is between $x = 0.30$ and 0.35 [7–9]. In the past decades, enormous research has been carried out to understand the MPB nature of ferroelectrics [10]. For higher concentrations, the PMN–PT system, shows FE T, R, monoclinic (M), and orthorhombic (O) phases at low temperature while a paraelectric cubic (C) phase is observed at high temperatures [2, 11]. Thus, PMN–PT materials with large PE, FE and pyroelectric properties and specific structure can be altered by the adjustment of composition. Out of various MPB systems like PZT and PZN–PT, the PMN–PT are extensively studied as it can be readily synthesized in a single crystal as well as ceramics forms. Different compositions are regularly used for various applications because of their high d_{33} and k_{33} coefficient. Wang et al. [12] showed the presence of C+T phases in MPB composition 0.6PMN–0.4PT. There are enormous works reported for PMN–PT with different motivations [13–15], however, dielectric,

impedance and modulus spectroscopy properties of $0.6Pb(Mg_{1/3}Nb_{2/3})O_3{-}0.4PbTiO_3$ (0.6PMN–0.4PT) ferroelectric ceramics over a wide frequency range have not been reported. Thus, in this study, the relaxation and conduction processes in 0.6PMN–0.4PT have been reported.

2. Experimental techniques

The precursor materials PbO, MgO, Nb_2O_3 and TiO_2 of M/s. CDH Pvt. Ltd. were carefully weighed. A homogeneous mixture was made by mixing in dry and methanol medium in mortar and pestle for 2 h followed by calcination at 950°C for 4 h. The lump obtained was re-grounded for 1 h and then pellets (12 mm diameter) were made by adding polyvinyl acetate (PVA) as binder and by pressing under a uniaxial pressure of 4 ton using hydraulic press. The pellets were then sintered at 1200°C for 4 h. For taking electrical measurement, either side of the pellet was painted with silver paint which was followed by heating at 150°C for 1 h. The structural measurement was carried out at room temperature (RT) using Rigaku Ultima IV diffractometer with Cu K_α radiation ($\lambda = 1.5405$ Å). Electrical parameters were measured by using a computer controlled impedance analyzer (HIOKI, IM 3570) in a wide frequency (1 Hz–4 MHz) and temperature (25–500°C) range.

3. Results and discussion

3.1. Structural analysis

The X-ray diffraction (XRD) profile of 0.6PMN–0.4PT is taken after the Rietveld refinement (see Fig. 1). The coexistence of both C as well as T phases with space groups of $Pm\text{-}3m$ and $P4mm$, respectively, are observed. The fitting is judged on the basis of peak to peak matching of observed and fitted data. However, the R-factors, i.e., R_{wp} (weighted profile), R_{exp} (statistically expected), and $\chi^2 = R_{wp}/R_{exp}$ are generally used to certify the quality of a fit [16]. A quality fit is found by

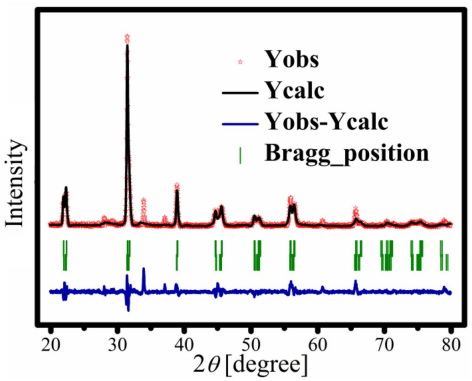

Fig. 1. XRD pattern of 0.6PMN–0.4PT.

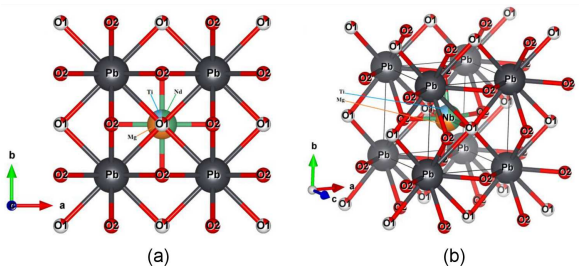

Fig. 2. (a, b) Structure scheme of 0.6PMN–0.4PT in different axis using VESTA crystallography software.

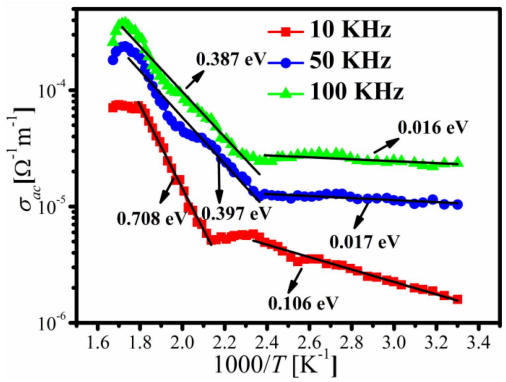

Fig. 3. Variation of σ_{ac} vs $10^3/T$ at 10, 50, and 100 kHz.

using the C+T phase model, where the smallest $\chi^2 = 5.43$, $R_{wp} = 14.1$ and $R_{exp} = 6.04$ value is obtained. The lattice parameters and unit cell volume obtained for C phase are found to be $a = b = c = 4.020$ Å and $V = 64.99$ Å^3 while for that of T phase is found to be $a = b = 3.977$ Å, $c = 4.061$ Å and $V = 64.22$ Å^3. Further, it is observed that the percentage of tetragonal phase in 0.6PMN–0.4PT is 88.35% while that of cubic phase is 11.65%.

Further, the schematic model (represented in Fig. 2a and b) is drawn using VESTA software by compiling the CIF file of refined data. It is observed that Pb^{3+} occupies the corner while Mg^{2+}, Nd^{5+} and Ti^{4+} occupied the body centre position of the unit cell. The obtained structure clearly matches with the previously reported results [3, 17, 18].

3.2. AC conductivity

Figure 3 shows the variation of ac conductivity (σ_{ac}) with $10^3/T$ of 0.6PMN–0.4PT at 10, 50, and 100 kHz. The σ_{ac} of the sample is calculated using the relation: $\sigma_{ac} = \omega\varepsilon_r\varepsilon_0 \tan(\delta)$, where symbols have their usual meaning. The plot σ_{ac} vs $10^3/T$ is fitted in the Arrhenius equation: $\sigma_{ac} = \sigma_0 \exp(-E_a/(k_B T))$ and activation energy (E_a) was calculated. Two distinct regions are linearly fitted; one at high temperatures where the curves appears to merge and other at low temperature. The values of E_a determined from the above relations

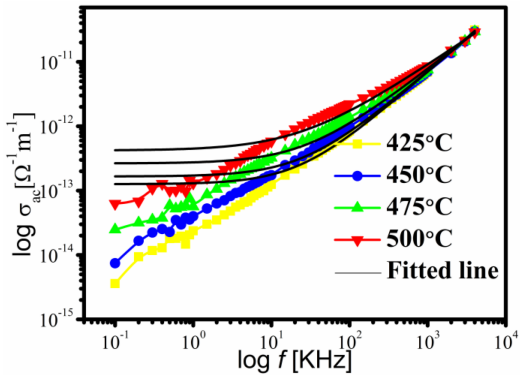

Fig. 4. Variation of $\sigma_{\rm ac}$ with frequency at the temperature range of 425–500°C.

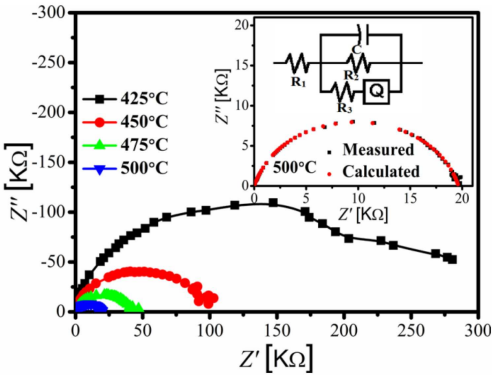

Fig. 5. Nyquist ($Z' - Z''$) plot at the temperature range of 425–500°C.

TABLE I

Parameters obtained from the fitting of Jonscher's power law (shown in Fig. 4.

	$\sigma_{\rm ac}$ [Ω^{-1} m^{-1}]	A	n	χ^2
225°C	9.69×10^{-5}	4.38×10^{-6}	0.99066	0.99986
250°C	2.18×10^{-4}	3.81×10^{-6}	0.99072	0.99989
275°C	4.7×10^{-4}	3.38×10^{-6}	0.99772	0.99978
300°C	4.35×10^{-4}	2.55×10^{-6}	0.99787	0.99977

at 10, 50, and 100 kHz are found to be 0.708, 0.397 and 0.39 eV respectively in the high-temperature region and 0.11, 0.02, and 0.02 eV in the low-temperature region. Since the value of E_a obtained is so small, it signifies that small amount of energy is sufficient to activate the charges for conduction. Further, E_a and $\sigma_{\rm ac}$ are found to decrease as frequency rises. This shows that the conduction of charges is due to hopping mechanism [19]. At lower frequencies, E_a is larger than that of high frequencies which is attributed to the effect of space charge polarization in the conduction mechanism. Different values of E_a in different regions are due to presence of ionic–polaronic and space charge in the conduction mechanism [19, 20].

The plot of σ_{ac} versus frequency is shown in Fig. 4. The frequency dependent electrical ac conductivity is explained by Jonscher's power law which is related to the dynamics of ionic hopping transport between localized sites and is given as $\sigma_{\rm ac}(\omega) = \sigma_{\rm dc} + A\omega^n$, where σ_{dc} is the frequency independent conductivity in the material, A is the pre-exponential factor. The values obtained from the fitting are listed in Table I. The value n gives information about the degree of interaction of charge carries with its environment. Generally, the value of n is in the range $0 \leq n \leq 1$ [21]. However, it is not a limited value below 1 as reported by Papathanassiou et al. [22]. For $n < 1$, it indicates that hopping of charge carriers are translational motion and $n > 1$, the motion is localised one. The ac conductivity is fitted with the power law through non-linear curve fit. It has been observed that for the whole range of temperatures the value of n is less than 1, thereby indicating the hopping of charge carrier is a translational motion. Further, variation of n with temperature gives information related to various theoretical models which plays an important role in understanding the conduction mechanism existing in the materials. In the studied sample it is observed that n increases with increase in temperature thus a non-overlapping small polaron tunneling (NSPT) model can be used [23].

3.3. Electrical study

Complex impedance spectroscopy (CIS) is distinctive, robust and non-destructive method for identifying some electrical responses in a broad series of frequency and temperature. The contribution of grain, grain boundary, interfacial resistance in modulus and other interconnected electrical parameters can be differentiated using this analysis. Various electrical properties such as impedance (Z) [24–28] and electric modulus (M) [29–31] are usually studied and can be expressed as

$$Z^* = Z' - jZ'' = R_s - \frac{\mathrm{i}}{\omega C_s}, \tag{1}$$

$$M^* = M' + \mathrm{i}M'' = \mathrm{i}\omega C_o Z^*, \tag{2}$$

where $\omega = 2\pi f$ represents angular frequency, C_o, R_s and C_s respectively signifies geometrical capacitance, resistance, and capacitance in series.

The Nyquist plot (Z' vs Z'') at 425–500°C is shown in Fig. 5. In the inset of Fig. 5, the equivalent circuit is fitted with ZSimWin software [32] at 500°C. The depressed semicircular arcs are found to decrease in diameter with rise in temperature thereby indicating the negative temperature coefficient of resistance (NTCR) behavior in the studied sample. The equivalent circuit used is $(R_1(CR_2(QR_3)))$ (inset) and fitting parameters are represented in Table II. In the equivalent circuit, R_1 (bulk resistance) existing in series with capacitance C and Q (capacitance due to grain) which in turn is parallel with R_2 (residual resistance) formed at interface. The constant phase element (CPE) [Q] is

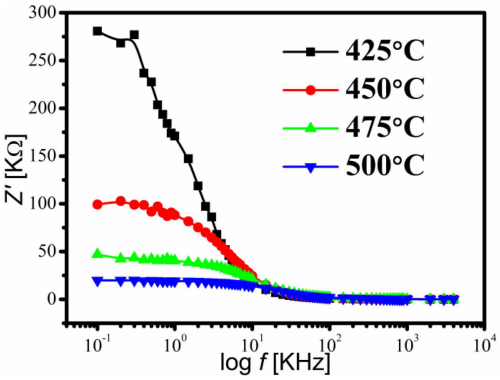

Fig. 6. Variation of Z' with frequency at the temperature range of 425–500°C.

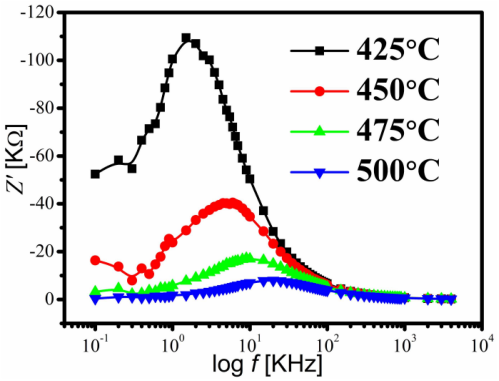

Fig. 7. Variation of Z'' with frequency at the temperature range of 425–500°C.

TABLE II

Fitting parameters corresponding to the equivalent circuit at 500°C (inset of Fig. 5).

Parameter	Value
R_1 [Ω]	2.79×10^7
C_1 [F]	3.38×10^{-6}
R_2 [Ω]	23.56
CPE [Q]	2.33×10^{-9}
Frequency power [n]	0.86
R_3 [Ω]	1.97×10^4
χ^2	2.12×10^{-4}

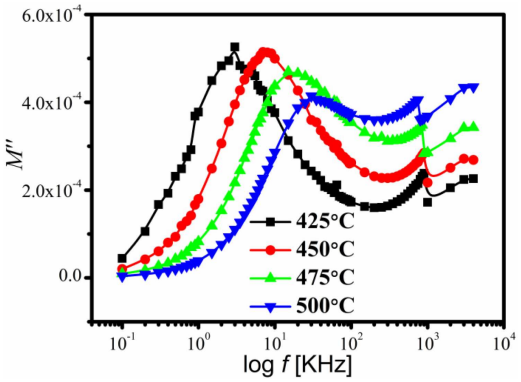

Fig. 8. Variation of M'' with frequency at the temperature range of 425–500°C.

in series with R_3 (grain resistance). The admittance of CPE is defined as $Y(\mathrm{CPE}) = A_0(\mathrm{i}\omega)^n$ where A_0 and n are temperature-dependent parameters and value of n ranges from 0 to 1.

The frequency dependence of Z' for a set of temperature is represented in Fig. 6 where Z' drops with increment in frequency and temperature. For selected temperatures, Z' values overlap at a higher frequency. Such behaviour is due to the liberation of space charge [31]. Further, at low frequency region, fall in the value of Z' with temperature reveals NTCR semiconducting behaviour [33, 34]. All the curves appear to coincide in high-frequency region, and then become independent of frequency.

Figure 7 represents the change in Z'' with frequency at 425–500°C where Z'' rises to reach the utmost value and then falls rapidly with a rise in temperature, there by suggesting the presence of relaxation phenomenon [34] which is further established by a rise in the width of the curve with temperature. At higher temperatures, the relaxation phenomenon originates owing to the occurrence of voids and imperfection. Further, at a low temperature, it is attributed to immobile species [28, 35].

For differentiating electrode polarization from grain boundary, phenomenon modulus analysis is done. Additionally, this analysis is convenient for investigating the bulk properties such as predictable conductivity relaxation time [36]. The influence of frequency on M'' over a set of temperatures is represented in Fig. 8. With an increase in temperature, M'' value shifts towards higher frequency regions. Such behaviour gives an idea that dielectric relaxation is activated thermally and also proves inherent domination of charge carrier in hopping mechanism [37]. Asymmetric increase in the modulus peaks suggests the growth of relaxation with distinct time constants, and thus a non-Debye type of relaxation is exhibited [26].

Influence of frequency on M' at 425–500°C is depicted in Fig. 9. In high frequency region, M' rises with frequency and reaches the highest asymptotical value for all temperatures which is attributed to absence of restoring force due mobile charge carriers [33]. Also M' attains a stable value at higher frequency for every temperature. This confirms the lack of sustainable electrode polarization in temperature domain [31].

Figure 10 represents the modulus spectrum at a set of temperatures. Irregular semicircular curve obtained before is now established by this method and seems to coincide for every temperature. This is possibly caused by the occurrence of electric relaxation phenomena. Semicircular arcs as necessary for the ideal Debye model are not formed. Instead they possess a distorted arc with centre appearing below

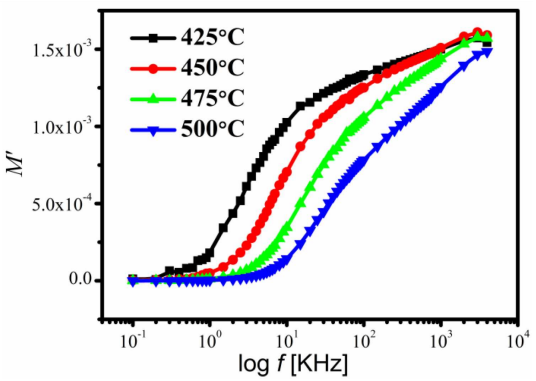

Fig. 9. Variation of M' with frequency at the temperature range of 425–500°C.

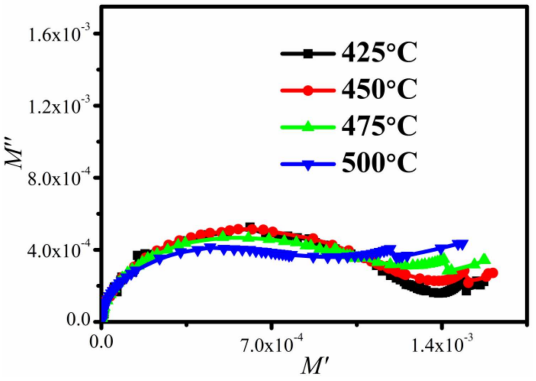

Fig. 10. Variation of M' with M'' at the temperature range of 425–500°C.

x-axis is observed which specifies the distribution of relaxation with distinct time constants. A single arc with its intercept on real axis in modulus plan shows the effect of bulk and grain boundaries to the overall capacitance. Additionally, M' vs frequency graph shows that effect of grain boundary is approximately 0 and has minor influence in the relaxation process.

4. Conclusion

0.6PMN–0.4PT is synthesized by the mixed oxide method. XRD analysis confirmed the biphasic structure of C+T phase with the space group of Pm-$3m$ and $P4mm$ respectively. Complex impedance plots show the effect of grains well as grain boundary in the sample. The grain and grain boundary resistance decreases with rise in temperature suggesting NTCR behavior in the studied sample. The sifting of modulus (M'') to higher frequency region indicated that the conduction process was possibly due to the hopping of charge carriers in the studied sample. The value of E_a of 0.6PMN–0.4PT is 0.71 eV at 10 kHz in the high-temperature region, which suggests the presence of ionic-polaronic and space charge in the conduction mechanism.

References

[1] S.W. Choi, T.R. Shrout, S.J. Jang, A.S. Bhalla, *Ferroelectrics* **100**, 29 (1989).

[2] D. Viehland, L. Ewart, J. Powers, J.F. Li, *J. Appl. Phys.* **90**, 2479 (2001).

[3] S.E. Park, T.R. Shrout, *J. Appl. Phys.* **82**, 1804 (1997).

[4] F. Wang, H. Wang, Q. Yang, Z. Zhang, K. Yan, *Ceram. Int.* **47**, 15005 (2021).

[5] F. Tian, Y. Liu, R. Ma, F. Li, Z. Xu, Y. Yang, *Appl. Acoust.* **175**, 107827 (2021).

[6] Q. Zhou, K.H. Lam, H. Zheng, W. Qiu, K.K. Shung, *Prog. Mater. Sci.* **66**, 87 (2014).

[7] Z.G. Dai, S.M. Dong, Z.H. Yin, F.Q. Li, Z.J. Zhai, J. Zhong, J.Y. Wang, *J. Synth. Cryst.* **34**, 1018 (2005).

[8] P. Kumar, O.P. Thakur, C. Prakash, T.C. Goel, *Physica B* **357**, 241 (2005).

[9] Yiping Guo, Haosu Luo, Di Ling, Haiqing Xu, Tianhou He, Zhiwen Yin, *J. Phys. Condens. Matter* **15**, L77 (2003).

[10] B. Noheda, D.E. Cox, G. Shirane, J. Gao, Z.-G. Ye, *Phys. Rev. B* **66**, 054104-10 (2002).

[11] B. Noheda, *Curr. Opin. Solid State Mater. Sci.* **6**, 27 (2002).

[12] H. Wang, J.-P. Laval, H. Ehrenberg, H. Fuess, S. Arrii-Clacens, H. Luo, B. Elouadi, *Ferroelectrics* **400**, 362 (2010).

[13] A. Benayad, G. Sebald, L. Lebrun, B. Guiffard, S. Pruvost, D. Guyomar, L. Beylat, *Mater. Res. Bull.* **41**, 1069 (2006).

[14] M. Algueró, A. Moure, L. Pardo, J. Holc, M. Kosec, *Acta Mater.* **5**, 501 (2006).

[15] K. Qian, B. Fang, Q. Du, J. Ding, X. Zhao, H. Luo, *Phys. Status Solidi A* **210**, 1149 (2013).

[16] L.B. Mccusker, R.B. Von Dreele, D.E. Cox, D. Louër, P. Scardi, *J. Appl. Crystallogr.* **32**, 36 (1999).

[17] Y. Namba, H. Takahashi, *CIRP Ann.* **59**, 589 (2010).

[18] H. Tan, H. Takenaka, C. Xu, W. Duan, I. Grinberg, A.M. Rappe, *Phys. Rev. B* **97**, 174101 (2018).

[19] Z. Imran, M.A. Rafiq, M.M. Hasan, *AIP Adv.* **4**, 067137 (2014).

[20] T. Sahu, B. Behera, *Trans. Electr. Electron. Mater.* **19**, 396 (2018).

[21] T. Sahu, A.K. Patra, B. Behera, *J. Alloys Compd.* **695**, 2273 (2017).

[22] A.N. Papathanassiou, I. Sokellis, J. Grammatikakis, *Phys. Lett.* **91**, 122911 (2007).

[23] T.M. Meaz, S.M. Attia, A.M. Abo El Ata, *J. Magn. Magn. Mater.* **257**, 296 (2003).

[24] S. Sen, R.N.P. Choudhary, *Mater. Chem. Phys.* **87**, 256 (2004).

[25] S. Brahma, R.N.P. Choudhary, A.K. Thakur, *Physica B* **355**, 188 (2005).

[26] J.R. Macdonald, *Impedance Spectroscopy Emphasizing Solid Materials and Systems*, Wiley, New York 1987.

[27] J. Suchanicz, *Mater. Sci. Eng. B* **55**, 114 (1998).

[28] C.K. Suman, K. Prasad, R.N.P. Choudhary, *J. Mater. Sci.* **41**, 369 (2006).

[29] V. Provenzano, L.P. Boesch, V. Volterra, C.T. Moynihan, P.B. Macedo, *J. Am. Ceram. Soc.* **55**, 492 (1972).

[30] H. Jain, C.H. Hsieh, *J. Non-Cryst. Solids* **172**, 1408 (1994).

[31] I.M. Hodge, M.D. Ingram, A.R. West, *J. Electroanal. Chem. Interf. Electrochem.* **58**, 429 (1975).

[32] B. Yeum, ZSimpWin Ver. 2.00, E Chem Software, 2001.

[33] S. Saparjya, S. Behera, B. Behera, P.R. Das, *J. Mater. Sci. Mater. Electron.* **28**, 3843 (2017).

[34] T. Sahu, B. Behera, *J. Mater. Sci. Mater. Electron.* **29**, 7412 (2018).

[35] T. Badapanda, S. Sarangi, B. Behera, S. Anwar, *Curr. Appl. Phys.* **14**, 1192 (2014).

[36] P.S. Das, P.K. Chakraborty, B. Behera, R.N.P. Choudhary, *Physica B* **395**, 98 (2007).

[37] B. Behera, P. Nayak, R.N.P. Choudhary, *Mater. Res. Bull.* **43**, 401 (2008).